

Surface Piezoelectricity of (0001) Sapphire

Alexandru B. Georgescu^{1,2,3,*} and Sohrab Ismail-Beigi^{1,2,4,5}


¹*Department of Physics, Yale University, New Haven, Connecticut 06520, USA*

²*Center for Research on Interface Structure and Phenomena, Yale University, New Haven, Connecticut 06520, USA*

³*Center for Computational Quantum Physics, The Flatiron Institute, 162 5th Avenue, New York, New York 10010, USA*

⁴*Department of Applied Physics, Yale University, New Haven, Connecticut 06520, USA*

⁵*Department of Mechanical Engineering and Materials Science, Yale University, New Haven, Connecticut 06520, USA*

 (Received 25 March 2018; revised manuscript received 30 April 2019; published 27 June 2019)

Interfaces of sapphire are of technological relevance as sapphire is used as a substrate in electronics, lasers, and Josephson junctions for quantum devices. In addition, its surface is potentially useful in catalysis. Using first-principles calculations, we show that, unlike bulk sapphire, which has inversion symmetry, the (0001) sapphire surface is piezoelectric. The inherent broken symmetry at the surface leads to a surface dipole and a significant response to imposed strain: the magnitude of the surface piezoelectricity is comparable to that of bulk piezoelectrics.

DOI: [10.1103/PhysRevApplied.11.064065](https://doi.org/10.1103/PhysRevApplied.11.064065)

I. INTRODUCTION

The surface of sapphire (α -Al₂O₃) as well as interfaces between sapphire and other materials have a wide range of electronic or optical applications. With sapphire as a substrate for the two-dimensional (2D) topological insulator stanene [1,2] and 2D transition-metal dichalcogenides [3], strain effects at the interface are likely to be important. Vibrational modes at the sapphire surface are also likely to couple to vibrational modes in 2D transition-metal dichalcogenides, which affects their properties, particularly charge-density waves and superconductivity [3]. In quantum-computing devices based on superconductors, alumina plays a critical part in forming the Josephson junctions [4], and interfacial electron-lattice coupling may provide an important loss mechanism. The mechanoelectric coupling between surface vibrational modes—possibly related to the surface piezoelectricity—and a piezoelectric was used to overcome the loss mechanism at the interface between sapphire and aluminum and to design a new type of quantum device [5]. Finally, another application of sapphire interfaces (in this case with gold) is in femtosecond-pulse lasers [6,7].

Separately and recently, the surface of sapphire has been shown to be useful for catalysis. The hydrophilic nature of aluminum-terminated α -Al₂O₃(0001) was exploited to create a scheme for achieving high selectivity in direct

conversion of methane to methanol [8], one of the most important goals in present-day catalysis. The hydrophilicity of this surface has been traced to lone-pair–surface bonds [9], and the extent of the surface aluminum displacement dictates the interaction of this surface with these technologically relevant molecules.

In an ultrahigh vacuum or in an O₂-only atmosphere, the aluminum-terminated sapphire (0001) surface is the stablest termination [8,10]. The Al “dangling bond” at this surface determines many of its properties [11–17] through changes in the aluminum position. In the presence of water, the Al-terminated surface becomes hydroxylated [10,14,18,19]. Nonetheless, with increased temperature and low H₂O pressure, the Al-terminated α -Al₂O₃(0001) is again stabilized.

In this work, we use density-functional theory to investigate the surface polarity, the surface dipole, and how the strain response of the dipole leads to a significant surface piezoelectric effect for both the Al-terminated surface and the hydroxylated surface of α -Al₂O₃(0001). The broad use of Al₂O₃ as well as recent developments in studying surface piezoelectricity in other materials [11] make a study of the piezoelectricity in sapphire an interesting and useful task. In addition, the corundum structure is found in many other materials, and the mechanism presented here may be of general interest. In connection with the aforementioned applications of sapphire, our work can provide a possible microscopic explanation of the efficiency of the aforementioned mechanoelectric quantum devices based

*ageorgescu@flatironinstitute.org

on surface piezoelectric coupling, highlight new directions for potential modification and control of polarization-driven surface chemistry [9], and provide insight into strain-driven changes in the electronic structure of 2D overlayers due to surface piezoelectric response.

II. METHODS

Our calculations are performed using density-functional theory [20,21] with the local-density approximation (LDA) [21,22] using the QUANTUM ESPRESSO software package [23] with ultrasoft pseudopotentials [24]. For electronic smearing, we use a Marzari-Vanderbilt [25] smearing width of 0.02 Ry (although all systems are robust insulators). We use a plane-wave cutoff of 35 Ry for the wave functions and 280 Ry for the electron density. The k -point sampling uses an $8 \times 8 \times 2$ grid for the bulk and an $8 \times 8 \times 1$ grid for the slab simulations. We vary the in-plane strain on our structures between -1% and $+1\%$ to measure the effective out-of-plane piezoelectric response. In the Appendix, we show that this level of strain is well within the linear regime for this material. Calculations of the bulk dielectric screening and Born effective charges use the Berry phase method combined with the finite-field approach [26,27].

We describe bulk Al_2O_3 using six formula units (a 30-atom cell) with a 4.76-\AA in-plane (x - y) lattice constant (19.4-\AA^2 in-plane unit-cell area) and a z lattice constant of 12.99 \AA : these are theoretical lattice constants that optimize the bulk total energy. To simulate surfaces, we perform slab simulations using the bulk in-plane lattice constants. Our slabs have either 30 atoms per unit cell (six structural units thick) or 60 atoms per unit cell. We use 30 \AA of vacuum added in the z direction to isolate the slabs. The Al-terminated (0001) surface we use (see Fig. 1) ensures two identical surfaces, no net dipole for the entire simulation cell, and no stray electric fields in the vacuum region. While previous studies found that simulating three structural units of the surface is sufficient for a good physical picture of the surface of sapphire [16], our thicker slabs permit us to carefully converge the relatively small displacements that penetrate into the subsurface regions. Furthermore, we study the hydroxylated (0001) surface, for which we follow the same philosophy: starting with the aforementioned alumina slab, we add H_2O symmetrically on both sides to generate two identical surfaces. This results in a 66-atom slab when we add H_2O to the 60-atom alumina slab.

III. RESULTS

A. Al-terminated surface

Our results on the surface structure of Al-terminated $\text{Al}_2\text{O}_3(0001)$ agree with prior literature. We find a bond shortening between the surface Al and the first layer of

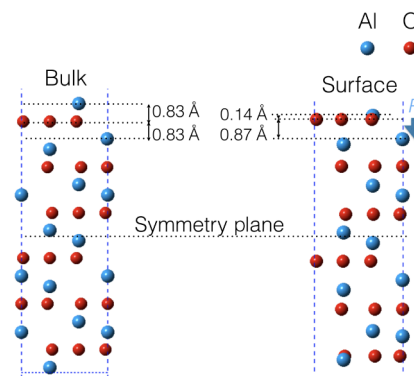


FIG. 1. Structures of bulk Al_2O_3 (left) and the relaxed 30-atom Al-terminated slab structure (right). The (0001) direction is vertical. Both systems have a symmetry plane ensuring zero net dipole and no long-range polar effects. The bulk has zero polarization by symmetry, while the surface of the slab has strong relaxations leading to a surface dipole. Key surface layer separations are labeled, and the direction of surface dipole is indicated by the arrow.

O [11–16] (see Fig. 1) that is polar and would, under atmospheric conditions, be hydroxylated due to its polarity [14, 18, 19]. Here, our objective is to go beyond this and analyze the dependence of this polarity on applied stress.

In Fig. 1, we show the structure of the bulk and our 30-atom slab. The bulk structural unit along (0001) is most easily understood as starting with an Al layer, followed by three O atoms in the second layer, and ending with another Al layer. Effectively, this forms two equal dipoles pointing from the O layer to the Al layers of opposite directions, which reflects the inversion symmetry of the bulk. For direct comparison with the slab results, we replicated the basic repeating unit six times when showing the bulk structure in Fig. 1. This choice of structural unit is nonpolar along (0001), automatically and correctly ensuring no piezoelectric response for the bulk.

To better understand the nature of the surface relaxations, we divide the top half of the slab into its structural units as shown in Fig. 2. The relaxations of the top Al layer are very large (0.69-\AA inward motion of the top Al layer as per Fig. 1): the surface Al has no O to bond to above it, so it moves into the surface to strengthen its available Al—O bonds. This strong distortion foreshadows a sizable response to perturbations. The layer-dependent Al—O z separations are given in Table I: each structural unit becomes distorted due to its proximity to the surface, but the magnitude of the perturbations decays rapidly as we go into the material.

We begin with the simplest physical approach that provides order-of-magnitude estimates of the dipole developed due to surface relaxation and strain. We sum the bulk Born effective (dynamical) charges Z^* of the ions multiplied by the ionic displacements to compute dipoles. Bulk Born effective charges are defined under periodic

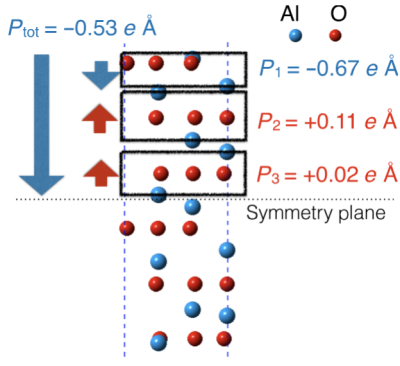


FIG. 2. Surface dipole moments of the (zero-strain) Al_2O_3 surface in the 30-atom slab with respect to the corresponding bulk configuration. Each five-atom structural unit is enclosed by a black rectangle. The first structural unit from the vacuum unit has the largest polarization. Screened bulk Born effective charges are used to compute the vertical components of the dipoles.

electrostatic boundary conditions, while our slab has no such periodicity along z , and hence the appropriate charges to use are the screened Born charges $\tilde{Z}^* = Z^*/\epsilon_\infty$, where ϵ_∞ is the optical (clamped-ion) dielectric constant: this reflects the fact that the electrons can, and will, screen the dipole formed by moving an ion in the slab geometry. We find, using the Berry phase approach, the bulk values $Z_{\text{Al}}^* = +2.92$, $Z_{\text{O}}^* = -1.94$, and $\epsilon_\infty = 3.20$, which agree well with prior LDA results [28]. Replacing Z^* by formal charges Al^{3+} and O^{2-} is a good approximation due to the strongly ionic nature of the material, but ignoring the electronic screening ϵ_∞ leads to large errors. Figure 2 and third column in Table II show dipoles formed per structural unit when using \tilde{Z}^* (numerically $+0.913$ for

TABLE I. Separation along z of Al planes and their neighboring O planes within the same structural units of the 60-atom slab. Structural units are counted as starting at the surface and going into the slab. Negative strain is compressive and positive strain is tensile.

Structural unit	Atomic plane	+1% strain	No strain	-1% strain
1	Al—O	0.112 Å	0.143 Å	0.173 Å
1	O—Al	0.852 Å	0.873 Å	0.893 Å
2	Al—O	0.997 Å	0.999 Å	1.002 Å
2	O—Al	0.872 Å	0.876 Å	0.881 Å
3	Al—O	0.840 Å	0.849 Å	0.858 Å
3	O—Al	0.815 Å	0.828 Å	0.841 Å
4	Al—O	0.815 Å	0.829 Å	0.842 Å
4	O—Al	0.824 Å	0.836 Å	0.848 Å
5	Al—O	0.826 Å	0.837 Å	0.849 Å
5	O—Al	0.825 Å	0.837 Å	0.849 Å
6	Al—O	0.825 Å	0.837 Å	0.849 Å
6	O—Al	0.825 Å	0.837 Å	0.849 Å

TABLE II. Strain-dependent (0001) dipoles (relative to the bulk) for each structural unit of the $\text{Al}_2\text{O}_3(0001)$ slab with 60 atoms as well as their sum. Negative strain is compressive and positive strain is tensile. Biaxial strain is imposed in the x - y plane. Screened bulk Born effective charges are used to compute the dipoles.

Structural unit	+1% strain	No strain	-1% strain
1	$-0.675 e \text{ \AA}$	$-0.666 e \text{ \AA}$	$-0.657 e \text{ \AA}$
2	$+0.114 e \text{ \AA}$	$+0.112 e \text{ \AA}$	$+0.110 e \text{ \AA}$
3	$+0.023 e \text{ \AA}$	$+0.019 e \text{ \AA}$	$+0.015 e \text{ \AA}$
4	$-0.008 e \text{ \AA}$	$-0.007 e \text{ \AA}$	$-0.005 e \text{ \AA}$
5	$+0.0005 e \text{ \AA}$	$+0.0005 e \text{ \AA}$	$+0.0004 e \text{ \AA}$
6	$+0.0002 e \text{ \AA}$	$+0.0002 e \text{ \AA}$	$+0.0002 e \text{ \AA}$
Sum	$-0.545 e \text{ \AA}$	$-0.541 e \text{ \AA}$	$-0.536 e \text{ \AA}$

Al^{3+} and -0.606 for O^{2-}). The large downward dipole of the topmost (surface) unit is partially canceled by the smaller upward responses of the units below it.

Next we use the screened effective charges to address the effect of strain. The strain can be due to static perturbations (e.g., epitaxy with a substrate or imposed static mechanical stress) or dynamical drive (e.g., acoustic sound waves or dynamic stresses). We change both in-plane x - y lattice parameters biaxially by the same amount and recompute the relaxed structure and layer-by-layer dipoles along z as shown in Table II. Changing from -1% (compressive) to $+1\%$ (tensile) leads to a 1.7% decrease in the magnitude of the net dipole moment across the entire surface region. If we ascribe this dipole to a region of thickness 2.17 Å, corresponding to the height of one bulk structural unit in the z direction, then we can estimate a piezoelectric coefficient in a unit appropriate for comparison with bulk materials. We find $-3.4 \times 10^{-3} \text{ C/m}^2$ for the change in polarization (dipole per volume) and piezoelectric coefficient $e_{31} = -0.088 \text{ C/m}^2$ (using Voigt notation and engineering strain convention). The negative sign means the net surface dipole becomes more positive with compressive strain, which, as per Table I, is primarily due to the surface Al cation moving outward (figuratively, it “pops out” due to being “squeezed” by its inward-moving O neighbors).

To ensure that our results are robust, we also perform calculations using the same method with the generalized gradient approximation exchange-correlation functional, and find that the change is minor (a 3% increase in the piezoelectric coefficient). Separately, while the specific numerical value of e_{31} depends on the equivalent thickness chosen (2.17 Å above), the rapid decay of dipoles shown in Fig. 2 and Table II means that the appropriate thickness is close to the height of a single bulk structural unit.

The above analysis provides a physical understanding of the surface response and semiquantitative results. A more-quantitative calculation based on Born effective charges requires the incorporation of changes to the values of

\tilde{Z}^* for the ions near the surface via cumbersome explicit calculations. We find that \tilde{Z}^* of the ions at or near the surface is reduced from bulk values. For the Al cations with their larger valence atomic orbitals, the Al atoms in the first three layers have their \tilde{Z}^* reduced by approximately 10%–15% (for deeper layers the values are within 3% of bulk values). For the O anions with their smaller valence atomic orbitals, the O in the surface layer suffers an 18% reduction of \tilde{Z}^* , while for the deeper layers the values are within 1% of the bulk value. Figures 3 and 4 present these trends graphically by displaying the changes of electron density when individual ionic layers are moved: the shift of electron density is much wider when Al cations compared with O anions are moved, and the convergence to the bulk distribution is much faster for O than for Al (also shown numerically in the captions).

Qualitatively, that the surface region shows reduced \tilde{Z}^* values is sensible since the band gap near the surface is

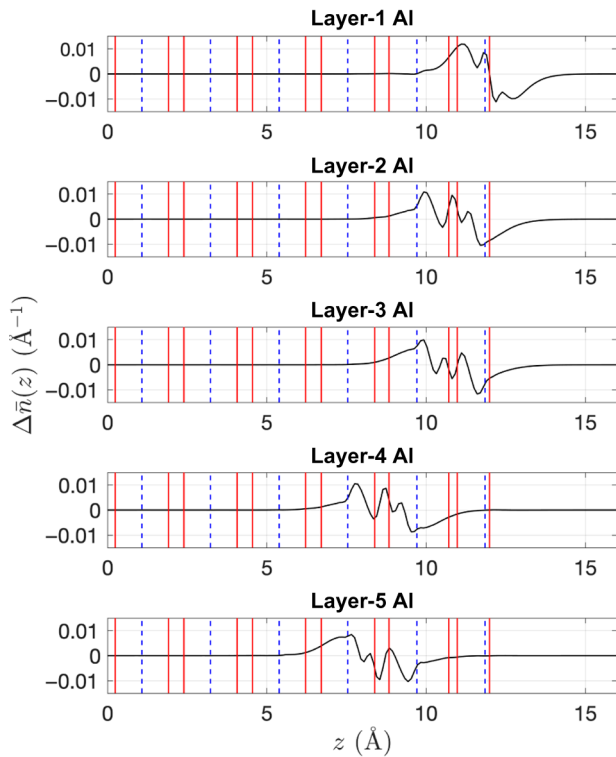


FIG. 3. Plane-averaged change of electron density due to displacement of Al ions by $\delta z = +0.01$ Å near the surface of $\text{Al}_2\text{O}_3(0001)$ in each two-dimensional atomic plane. Layer 1 is the surface Al layer, and increasing layer numbers move into the material. Black curves show the change of electron density (averaged in the x - y plane). Vertical solid red lines indicate the z coordinates of Al planes, while blue vertical dashed blue lines indicate z positions of O planes. The origin is the center of the slab. The electron-density changes (combined with the motion of the ionic core and nucleus) correspond to effective charges of $+0.83$, $+0.77$, $+0.81$, $+0.89$, and $+0.94$ when going from layer 1 to layer 5, which are to be compared with the screened bulk value of $+0.913$.

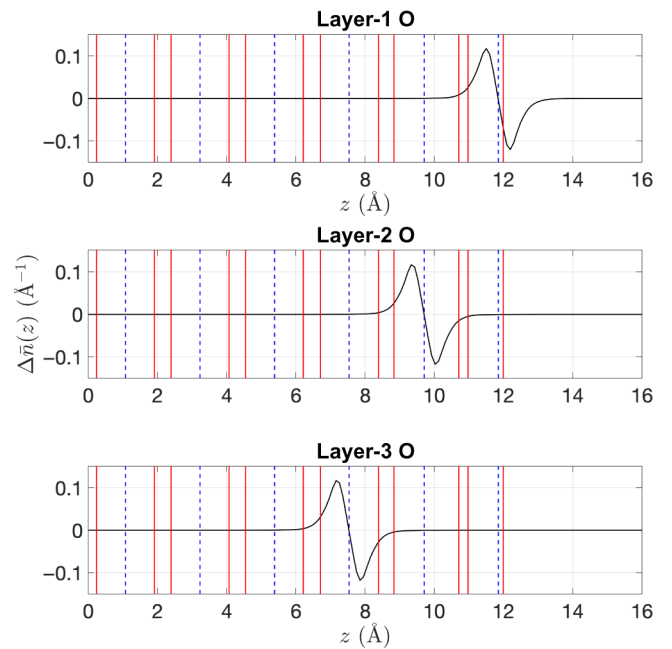


FIG. 4. Plane-averaged change of electron density due to displacement of O ions by $\delta z = +0.01$ Å near the surface of $\text{Al}_2\text{O}_3(0001)$ in each two-dimensional atomic plane. The nomenclature is the same as for Fig. 3. The electron-density changes (combined with the motion of the ionic core and nucleus) correspond to effective charges of -0.50 , -0.61 , and -0.61 when going from layer 1 to layer 3, which are to be compared with the screened bulk value of -0.606 .

smaller than the bulk and broken/dangling bonds at the surface are more polarizable. To understand this point in more detail, Figs. 5 and 6 display the nature of the conduction-band and valence-band edges of the unstrained (relaxed) alumina slab. The conduction-band-edge state is localized almost exclusively on the surface Al layer with a directional “dangling” out-of-surface shape, while the valence-band-edge state is a superposition of O $2p$ states that are localized on the surface layer and the subsurface layer. Hence, the band-edge states are indeed localized on the surface. Furthermore, we expect the conduction-band-edge state to be much more sensitive to the existence of the surface than the valence-band-edge state. We corroborate this sensitivity by computing the change of energy of the band edges on formation of the surface. The LDA band gap of the slab is 4.8 eV, which is 1.6 eV lower than the LDA bulk band gap of 6.4 eV. By using the minimum energy of the localized O $2s$ band as an energy reference, we find that the band-gap reduction is essentially due to the conduction-band edge dropping in energy by approximately 1.5 eV (while the valence-band edge rises by a small amount of approximately 0.04 eV). The lowering of the conduction-band-edge energy is sensible since the surface Al cations have reduced coordination: the removal of O nearest neighbors reduces the electrostatic (Madelung) repulsive potential felt by electrons at the Al sites; in parallel,

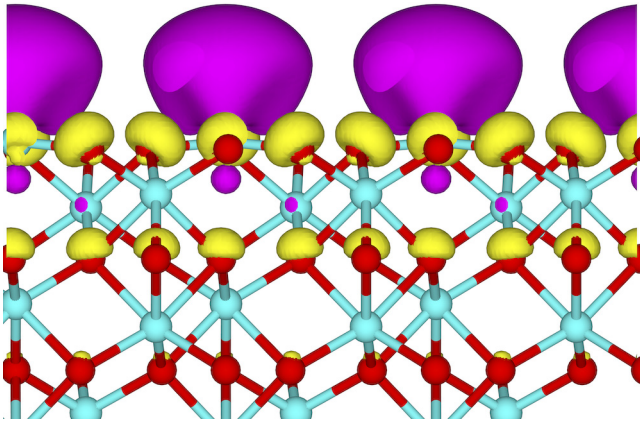


FIG. 5. Isosurface plot of the conduction-band-edge wave function of the unperturbed (relaxed) Al_2O_3 surface. Purple indicates a positive value and yellow indicates a negative value of the same magnitude. The state is strongly localized on the surface Al and shaped much like “dangling” orbitals pointing out of the surface.

removal of Al—O bonds for the surface Al cations reduces the antibonding character, and thus lowers the energy, of the Al-dominated conduction-band states.

However, instead of our pursuing a cumbersome approach based on screened effective charges, the slab geometry with a vacuum permits us to compute the change of surface dipole in two independent and straightforward ways using the electron density itself. First, the *ab initio* calculations provide us with the total charge density ρ , and since we have a vacuum in our unit cell, where ρ essentially drops to zero, computation of the total dipole $p_z = \int d^3r z \rho$ in the surface region of the slab is straightforward. To do this, the integral is replaced by a discrete sum over the real-space grid used in the calculation, and to find consistent results, we decompose the sum over the surface layers of one side of the slab into a sum of dipolar contributions from contiguous material units, where each unit has a pseudo-electron-density integrating

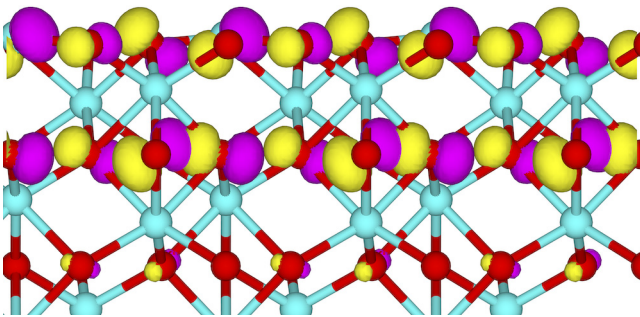


FIG. 6. Isosurface plot of the valence-band-edge wave function of the unperturbed (relaxed) Al_2O_3 surface. Purple indicates a positive value and yellow indicates a negative value of the same magnitude. The state is essentially of pure O $2p$ character and is localized primarily on the surface and subsurface oxygen layers.

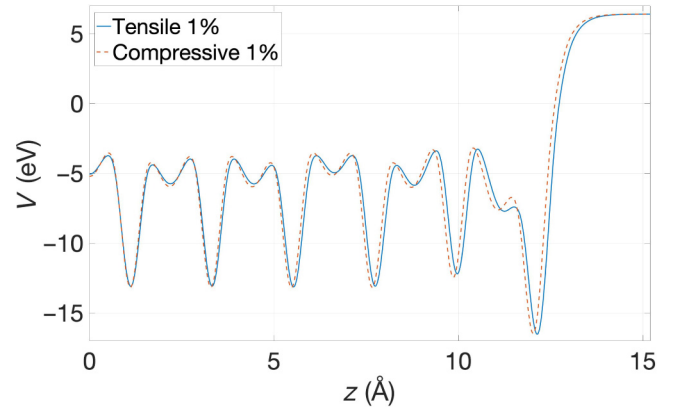


FIG. 7. Plane-averaged electrostatic potential along z for 1% tensile strain and 1% compressive strain, with $z = 0$ defined to be the center of the slab, and the surface is at $z \approx 13$ Å. The potential in the vacuum is shifted so that it has the same value for the two strain states. The change in electrostatic potential described in the main text is obtained by taking the difference of potentials at $z = 0$.

24 pseudo-valence-electrons (the correct number for one Al_2O_3 unit); after the first few surface units, the dipole for each further unit is essentially zero (as is necessary from the symmetry of bulk sapphire) and we terminate the integration. By computing the change of this dipole between the 1%-tensile-strain state and the 1%-compressive-strain state, we obtain a change of polarization equal to -6.1×10^{-3} and $e_{31} = -0.16$ C/m².

Second, using basic electrostatics, in a parallel-plate geometry such as in our slab calculation, a dipole along z will create a potential drop across it, and if we examine the change of potential versus strain, we can obtain the change of dipole. Hence, we align the central symmetry plane of the slabs in all our calculations and compute the electrostatic potential for each simulation averaged in the x - y plane. We then take the difference between the potential on the symmetry plane at the center of our slab and deep in the vacuum, where the potential is constant. Figure 7 shows the two potential profiles. The strain dependence of this potential difference is then computed. Between the -1% -strain and $+1\%$ -strain states examined, we find a net potential difference of approximately 0.16 V. A parallel-plate model together with an assumed thickness of 2.17 Å gives us a net change of polarization of -6.5×10^{-3} C/m². This translates into $e_{31} = -0.17$ C/m².

B. Hydroxylated surface

Our final set of results concern the effect of changing the surface termination. To examine this effect, we consider the hydroxylated Al-terminated (0001) sapphire surface with an H_2O coverage of one H_2O molecule per primitive surface unit cell. This surface has been studied by both theory and experiment [18,19,29], and it is known that the

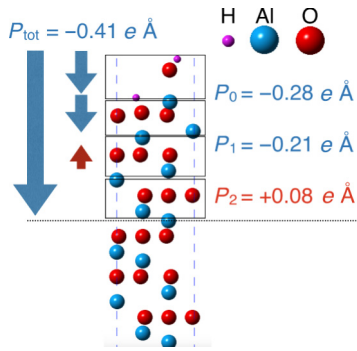


FIG. 8. Surface structure and dipole moments of the zero-strain and relaxed hydroxylated Al_2O_3 surface in the 30-atom slab with respect to the corresponding bulk configuration. The surface water molecule followed by the first three unit cells of Al_2O_3 are framed with black triangles. The water molecule and the first sapphire unit cell have the largest dipole moment. Screened bulk Born effective charges are used.

H_2O molecule dissociates into a hydroxide anion (OH^-) that bonds via its O to the surface Al cation and an H^+ cation that bonds to an oxygen anion in the layer immediately below the terminating Al layer. The structure of the surface region is shown in Fig. 8 along with the dipoles of the various structural units. Table III gives the vertical separations of cations and anions for the hydroxylated surface (for all three strain values), and Table IV gives the dipoles of the structural units at and near the surface.

We begin with the observation that, due to being capped by the OH^- , the surface Al is pulled out of the surface compared with the clean Al-terminated case. Next, despite the higher position of the Al cation, the net surface dipole

TABLE III. Separation along z of cations and anions for the hydroxylated surface for each structural unit of the 66-atom slab: the surface H_2O is structural unit zero, the remaining structural units are the same as for the Al-terminated surface. Negative strain is compressive and positive strain is tensile. The values listed for structural units 1–5 are averages over the three inequivalent oxygen anions in each structural unit.

Structural unit	Atomic plane	+1% strain	No strain	−1% strain
0	H—O	0.578 Å	0.583 Å	0.586 Å
0	O—H	1.435 Å	1.477 Å	1.517 Å
1	Al—O	0.650 Å	0.669 Å	0.687 Å
1	O—Al	0.879 Å	0.890 Å	0.901 Å
2	Al—O	0.918 Å	0.921 Å	0.925 Å
2	O—Al	0.827 Å	0.838 Å	0.849 Å
3	Al—O	0.815 Å	0.827 Å	0.841 Å
3	O—Al	0.820 Å	0.832 Å	0.845 Å
4	Al—O	0.823 Å	0.834 Å	0.847 Å
4	O—Al	0.825 Å	0.837 Å	0.849 Å
5	Al—O	0.825 Å	0.837 Å	0.849 Å
5	O—Al	0.825 Å	0.836 Å	0.848 Å

TABLE IV. Strain-dependent (0001) dipoles (relative to the bulk) for each structural unit of the hydroxylated surface of the 66-atom slab. Negative strain is compressive and positive strain is tensile. Biaxial strain is imposed in the x - y plane. Screened bulk Born effective charges are used.

Structural unit	+1% strain	No strain	−1% strain
0	$-0.268 e \text{ \AA}$	$-0.272 e \text{ \AA}$	$-0.283 e \text{ \AA}$
1	$-0.209 e \text{ \AA}$	$-0.202 e \text{ \AA}$	$-0.195 e \text{ \AA}$
2	$+0.083 e \text{ \AA}$	$+0.076 e \text{ \AA}$	$+0.070 e \text{ \AA}$
3	$-0.004 e \text{ \AA}$	$-0.004 e \text{ \AA}$	$-0.004 e \text{ \AA}$
4	$-0.002 e \text{ \AA}$	$-0.002 e \text{ \AA}$	$-0.002 e \text{ \AA}$
5	$+0.001 e \text{ \AA}$	$+0.001 e \text{ \AA}$	$+0.000 e \text{ \AA}$
Sum	$-0.394 e \text{ \AA}$	$-0.403 e \text{ \AA}$	$-0.413 e \text{ \AA}$

for the hydroxylated surface points inward just as for the Al-terminated case. But this time, the net inward dipole is dominated by the dipole contribution of the dissociated H_2O unit: as is visible from Fig. 8, H^+ sits well below OH^- , resulting in a large net-negative-dipole contribution.

However, although both surface terminations have a net negative dipole, their strain responses have opposite signs: unlike the Al-terminated case, compressive strain on the hydroxylated surface results in a more-negative surface dipole. Examining the individual structural-unit contributions in Table IV, we see that the alumina subsystem behaves similarly to the clean Al-terminated case: its net dipole becomes more positive with compressive strain. However, the response of the surface H_2O unit is negative and larger in magnitude, leading to a net negative response. Analysis of the layer-by-layer vertical separations and their strain response paints the following picture: the surface Al moves up with compressive strain, and this in turn moves its capping OH^- rigidly upward (“riding” behavior); however, H^+ does not move much since it is bound to the next subsurface O layer. The net effect is to increase the vertical separation between H^+ and OH^- and create a more-negative surface dipole.

For a numerical estimate of the surface piezoelectric response, we use screened Born effective charges. For Al and O, we use the same values as we used for the Al-terminated surface, while the screened Born effective charge of H is fixed by the neutrality of an H_2O molecule (i.e., $2\tilde{Z}_{\text{H}}^* + \tilde{Z}_{\text{O}}^* = 0$). These effective charges are used to compute the dipoles shown in Fig. 8 and Table IV. This approach leads to an estimated value of $e_{31} = +0.18 \text{ C/m}^2$. For a more-numerically-accurate value than can be provided by bulk screened Born effective charges, we apply the dipole-integration method described above to the hydroxylated case. The result is $e_{31} = +0.16 \text{ C/m}^2$ for the hydroxylated surface.

IV. DISCUSSION

For the surface piezoelectric response coefficient of (0001) sapphire we find $|e_{31}| \sim 0.1 \text{ C/m}^2$. This is

comparable with the values for workhorse bulk piezoelectric materials such as ZnO with $e_{31} = 0.53 \text{ C/m}^2$, LiNbO₃ with $e_{31} = 0.37 \text{ C/m}^2$, AlN with $e_{31} = 0.58 \text{ C/m}^2$, and BaTiO₃ with $e_{31} = 2.16 \text{ C/m}^2$ [30,31]. Hence, the piezoelectricity of the (0001) surface of Al₂O₃ is comparable in strength to that of a unit cell of typical bulk crystalline piezoelectric materials.

One may also compare our results with appropriately defined surface piezoelectric coefficients from first-principles theory [11,32]. For a bulk piezoelectric material such as ZnO, its (0001) surface has a surface piezoelectric constant of $1.0 \times 10^{-10} \text{ C/m}$, while the surfaces of nonpiezoelectric phases have surface piezoelectric constants that are about 10 times smaller [11]. For comparison, our Al-terminated Al₂O₃(0001) surface has a constant of $3.7 \times 10^{-11} \text{ C/m}$, which is again comparable.

If one seeks a simple order-of-magnitude estimate of $|e_{31}|$, one can use formal charges to compute the surface dipole of the relaxed zero-strain surface (a refined estimate screens the surface dipole by dividing by the optical dielectric constant ϵ_∞). Then, as Tables II and IV demonstrate, the change of dipole is roughly equal to the strain imposed times the dipole itself, yielding an easy estimate of the dipole response to strain. Hence, as long as the surface structure of an ionic material is known (through experiment and/or theory), one can quickly provide a ballpark estimate of the strength of the surface piezoelectric response.

With regard to surface termination effects in experimental situations, while the clean Al-terminated surface and the hydroxylated surface we modeled have e_{31} coefficients of opposite sign, the hydroxylated case examined corresponds to the maximum surface coverage for chemisorbed H₂O. For lower concentrations of chemisorbed H₂O, we expect e_{31} to have the same sign and magnitude as that of the clean Al-terminated surface. In addition, for electronic or quantum-device applications, any H₂O on the surface can easily be driven off with modest temperature increases and vacuum conditions, leading to the clean Al-terminated case: we believe the Al-terminated surface to be relevant for such device applications. For catalytic applications in hydrated or aqueous conditions, the hydroxylated-surface response should be the dominant observed behavior. For either case, our simulations describe ordered crystalline surfaces: understanding the potential effect of surface disorder is more challenging from first principles and is beyond the scope of this work.

V. CONCLUSION

Our calculations predict that the (0001) surface of sapphire (Al₂O₃) has a strong structural response to strain that leads to surface piezoelectricity. Given the wide use of sapphire substrates in many scientific and technological fields, this result is important for understanding and

engineering these systems. Furthermore, our work illustrates a more-general situation where the surface of a centrosymmetric material can develop a significant piezoelectric response due to the broken translational symmetry, and our approach, analysis, and rules of thumb can be applied in a variety of other such materials.

ACKNOWLEDGMENTS

We thank Robert Schoelkopf and Peter T. Rakich for highlighting the importance of sapphire as a key platform for quantum devices. We thank Arvin Kakekhani, Frederick Walker, and Claudia Lau for helpful conversations during the writing of this work. The work done at Yale University was supported by the National Science Foundation via Grant No. MRSEC DMR 1119826. We thank the Yale Center for Research Computing for guidance and use of the research computing infrastructure. This work also used the Extreme Science and Engineering Discovery Environment, which is supported by National Science Foundation Grant No. ACI-1548562. This work used Extreme Science and Engineering Discovery Environment Comet supercomputer through Allocation No. MCA08X007, as well as the Flatiron Institute Iron Cluster. The Flatiron Institute is supported by the Simons Foundation.

APPENDIX

To check that our results do not strongly depend on the exchange-correlation functional we pick, we also perform calculations within the Perdew-Burke-Ernzerhof version of the generalized-gradient-approximation exchange-correlation functional [33], and compare the change in dipole with respect to the same change in strain ($\pm 1\%$) and obtain a minor increase in the estimated dipole change of 3%.

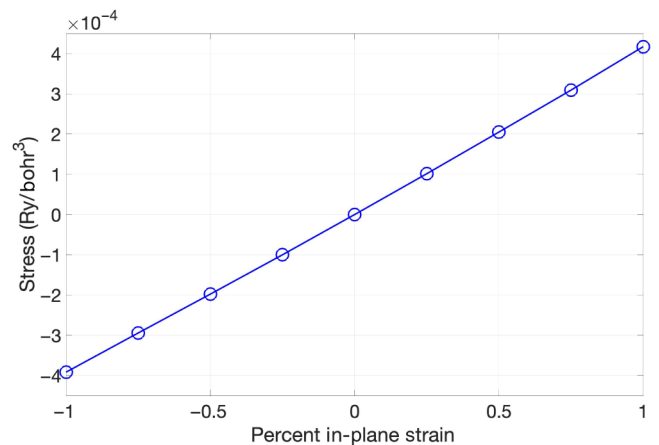


FIG. 9. Stress versus strain for bulk sapphire based on LDA calculations: compressive strain is positive and tensile strain is negative.

Furthermore, to check that our calculations are performed in the linear regime of the strain for bulk sapphire, we perform multiple bulk LDA calculations and plot the stress as a function of strain in Fig. 9, which shows that the results in the main text are safely in the linear (small-strain) regime.

-
- [1] H. Wang, S. T. Pi, J. Kim, Z. Wang, H. H. Fu, and R. Q. Wu, Possibility of realizing quantum spin Hall effect at room temperature in stanene/ Al_2O_3 (0001), *Phys. Rev. B* **94**, 035112 (2016).
- [2] M. Araidai, M. Kurosawa, A. Ohta, and K. Shiraishi, First-principles study on adsorption structure and electronic state of stanene on α -alumina surface, *Jpn. J. Appl. Phys.* **56**, 095701 (2017).
- [3] S. Manzeli, D. Ovchinnikov, D. Pasquier, O. V. Vazyev, and A. Kis, 2D transition metal dichalcogenides, *Nat. Rev. Mater.* **2**, 17033 (2017).
- [4] J. S. Tsai, Toward a superconducting quantum computer: Harnessing macroscopic quantum coherence, *Proc. Jpn. Acad. Ser. B Phys. Biol. Sci.* **86**, 275 (2010).
- [5] Y. Chu, P. Kharel, W. H. Renninger, L. D. Burkhardt, L. Frunzio, P. T. Rakich, and R. J. Schoelkopf, Quantum acoustics with superconducting qubits, *Science* **358**, 199 (2017).
- [6] D. E. Spence, P. N. Kean, and W. Sibbett, 60-fsec pulse generation from a self-mode-locked Ti:sapphire laser, *Opt. Lett.* **16**, 42 (1991).
- [7] S. Han, H. Kim, Y. W. Kim, Y. J. Kim, S. Kim, I. Y. Park, and S. W. Kim, High-harmonic generation by field enhanced femtosecond pulses in metal-sapphire nanostructure, *Nat. Commun.* **7**, 13105 (2016).
- [8] A. A. Latimer, A. Kakekhani, A. R. Kulkarni, and J. K. Nørskov, Direct methane to methanol: The selectivity-conversion limit and design strategies, *ACS Catal.* **8**, 6894 (2018).
- [9] A. Kakekhani, L. T. Røling, A. Kulkarni, A. A. Latimer, H. Abroshan, J. Schumann, H. Aljama, S. Siahrostami, S. Ismail-Beigi, F. Abild-Pedersen, and J. K. Nørskov, Nature of lone-pair-surface bonds and their scaling relations, *Inorg. Chem.* **57**, 7222 (2018).
- [10] Vi A. Ranea, Ian Carmichael, and William F. Schneider, DFT investigation of intermediate steps in the hydrolysis of α -Al O (0001), *Society* **113**, 2149 (2009).
- [11] S. Dai, M. Gharbi, Pr. Sharma, and H. S. Park, Surface piezoelectricity: Size effects in nanostructures and the emergence of piezoelectricity in non-piezoelectric materials, *J. Appl. Phys.* **110**, 104305 (2011).
- [12] J. Ahn and J. W. Rabalais, Composition and structure of the $\text{Al}_2\text{O}_3\{0001\} - (1 \times 1)$ surface, *Surf. Sci.* **388**, 121 (1997).
- [13] J. R. Heffelfinger, M. W. Bench, and C. B. Carter, Steps and the structure of the (0001) α -alumina surface, *Surf. Sci.* **370**, L168 (1997).
- [14] I. Batyrev, A. Alavi, and M. W. Finnis, Ab initio calculations on the Al_2O_3 (0001) surface, *Faraday Discuss.* **114**, 33 (1999).
- [15] I. Manassidis, A. de Vita, and M. J. Gillan, Structure of the (0001) surface of α - Al_2O_3 from first principles calculations, *Surf. Sci.* **285**, L517 (1993).
- [16] C. Verdozzi, D. R. Jennison, P. A. Schultz, and M. P. Sears, Sapphire (0001) Surface, Clean and with d-Metal Overlayers, *Phys. Rev. Lett.* **82**, 799 (1999).
- [17] C. F. Walters, K. F. McCarty, E. A. Soares, and M. A. Van Hove, Surface structure of α - Al_2O_3 determined by low-energy electron diffraction: Aluminum termination and evidence for anomalously large thermal vibrations, *Surf. Sci.* **464**, L732 (2000).
- [18] M. A. Nygren, D. H. Gay, C. Richard, and A. Catlow, Hydroxylation of the surface of the corundum basal plane, *Surf. Sci.* **380**, 113 (1997).
- [19] P. J. Eng, T. P. Trainor, G. E. Brown, G. A. Waychunas, M. Newville, S. R. Sutton, and M. L. Rivers, Structure of the hydrated α - Al_2O_3 (0001) surface, *Science* **288**, 1029 (2000).
- [20] P. Hohenberg and W. Kohn, Inhomogeneous electron gas, *Phys. Rev.* **136**, 864 (1964).
- [21] W. Kohn and L. J. Sham, Self-consistent equations including exchange and correlation effects, *Phys. Rev.* **140**, 1133 (1965).
- [22] J. P. Perdew and Alex Zunger, Self-interaction correction to density-functional approximations for many-electron systems, *Phys. Rev. B* **23**, 5048 (1981).
- [23] P. Giannozzi *et al.*, Quantum ESPRESSO: A modular and open-source software project for quantum simulations of materials, *J. Phys. Condens. Matter* **21**, 395502 (2009).
- [24] D. Vanderbilt, Soft self-consistent pseudopotentials in a generalized eigenvalue formalism, *Phys. Rev. B* **41**, 7892 (1990).
- [25] N. Marzari, D. Vanderbilt, A. De Vita, and M. C. Payne, Thermal Contraction and Disorder of the Al(110) Surface, *Phys. Rev. Lett.* **82**, 3296 (1999).
- [26] R. D. King-Smith and D. Vanderbilt, Theory of polarization of crystalline solids, *Phys. Rev. B* **47**, 1651 (1993).
- [27] I. Souza, J. Íñiguez, and D. Vanderbilt, First-Principles Approach to Insulators in Finite Electric Fields, *Phys. Rev. Lett.* **89**, 117602 (2002).
- [28] B. Montanari, B. Civalleri, C. M. Zicovich-Wilson, and R. Dovesi, Influence of the exchange-correlation functional in all-electron calculations of the vibrational frequencies of corundum, *Int. J. Quantum Chem.* **106**, 1703 (2006).
- [29] Z. Lodziana, J. K. Nørskov, and P. Stoltze, The stability of the hydroxylated (0001) surface of α - Al_2O_3 , *J. Chem. Phys.* **118**, 11179 (2003).
- [30] A. Jain, S. P. Ong, G. Hautier, W. Chen, W. D. Richards, S. Dacek, S. Cholia, D. Gunter, D. Skinner, G. Ceder, K. A. Persson, A. Jain, P. Ong, G. Hautier, W. Chen, D. Gunter, D. Skinner, G. Ceder, and K. A. Persson, Commentary: The materials project: A materials genome approach to accelerating materials innovation, *APL Mater.* **1**, 011002 (2013).
- [31] M. De Jong, W. Chen, H. Geerlings, M. Asta, and K. A. Persson, A database to enable discovery and design of piezoelectric materials, *Sci. Data* **2**, 150053 (2015).
- [32] S. Shen and S. Hu, A theory of flexoelectricity with surface effect for elastic dielectrics, *J. Mech. Phys. Solids* **58**, 665 (2010).
- [33] J. P. Perdew, K. Burke, and M. Ernzerhof, Generalized Gradient Approximation Made Simple, *Phys. Rev. Lett.* **77**, 3865 (1996).